Journal of Alloys and Compounds 737 (2018) 330–336

Contents lists available at ScienceDirect

Journal of Alloys and Compounds

journal homepage: http://www.elsevier.com/locate/jalcom

Intercalating petroleum asphalt into electrospun ZnO/Carbon nanofibers as enhanced free-standing anode for lithium-ion batteries

Qingshan Zhao [a, 1], Hui Xie [a, 1], Hui Ning [a], Jialiang Liu [a], Haoran Zhang [b], Luhai Wang [b], Xiaobo Wang [a], Yulong Zhu [a], Shangyue Li [a], Mingbo Wu [a, *]

[a] State Key Laboratory of Heavy Oil Processing, College of Chemical Engineering, China University of Petroleum (East China), Qingdao 266580, People's Republic of China
[b] Petrochemical Research Institute, Petro China Company Ltd., Beijing 102206, People's Republic of China

ARTICLE INFO

Article history:
Received 24 August 2017
Received in revised form
3 December 2017
Accepted 10 December 2017
Available online 11 December 2017

Keywords:
Electrospun
ZnO/Carbon nanofibers
Intercalate
Petroleum asphalt
3D conductive network
Lithium-ion batteries

ABSTRACT

In this study, we demonstrate novel 3D interconnected nanofiber films by intercalating petroleum asphalt into electrospun ZnO/carbon nanofibers (ZnO/CNFs-PA) as enhanced free-standing anode for lithium-ion batteries (LIBs). ZnO/CNFs composite is synthesized via one-step electrospinning of polyacrylonitrile and zinc acetate dehydrate. Through solvent impregnation and subsequent two-step thermal treatments, appropriate amount of petroleum asphalt (PA) is intercalated into ZnO/CNFs to generate a conductive carbon film between and around the nanofibers. Benefitting from the 3D conductive network established by the carbon nanofibers and PA-carbon layer, the as-prepared ZnO/CNFs-PA-1.0 film is evaluated as a free-standing LIBs anode and exhibits a promoted reversible capacity of 702 mA h g^{-1} at current density of 200 mA g^{-1}, associating with excellent cycling stability and rate performance. Such novel nanostructure can effectively accommodate the volume expansion of ZnO, facilitate charge transfer and reinforce the electrode. The present strategy is believed to provide a feasible method to produce transition metal oxide/carbon nanofibers electrodes with superior electrochemical performance for LIBs.

© 2017 Elsevier B.V. All rights reserved.

1. Introduction

With the rapid development of electronic devices and electric vehicles, as well as other renewable energy integrations, rechargeable lithium-ion batteries (LIBs) have attracted enormous attention as promising portable energy storage devices due to their high energy density, appropriate operating voltage and long lifespan [1]. Although graphite is mainly employed as the commercial LIBs anode material for its satisfactory stability, its limited theoretical capacity (372 mA h g^{-1}) [2] cannot meet the current and future demands for large energy and power densities. Therefore, various types of nanostructured anode have been developed through different synthesis technologies to achieve superior LIBs with high reversible capacity, good rate capability and cycling stability. Among these, the one-dimensional (1D) nanostructured materials [3] including nanotubes [4,5], nanofibers [6] and nanorods [7], etc. are prominent to achieve excellent electrochemical performance due to their unique morphology and properties.

Electrospinning technology has been developed as one of the most convenient, versatile, and cost-efficient methods to prepare 1D nanomaterials. By employing organic polymers as the precursor, carbon nanofibers (CNFs) with diameters ranging from nanometers to micrometers can be simply synthesized through electrospinning processes [8]. The unique 1D nanostructure endows CNFs large surface area and conductive channels for electron transport, which is beneficial to LIBs charge/discharge processes [9]. Various electrospun CNFs have been reported as promising anode materials for LIBs [10–12]. Very recently, simultaneously merging nanostructured transition metal oxides (TMOs) with high theoretical capacities into CNFs through electrospinning process has been proved to be an efficient approach to further increase the reversible capacity of initial CNFs [13,14]. Whereas severe volume changes and poor conductive characteristic of TMOs leads to poor stability and inferior rate capability, seriously hindering their practical applications. Coupling nanostructured TMOs with

* Corresponding author.
E-mail address: wumb@upc.edu.cn (M. Wu).
[1] These authors contributed equally to this work.

https://doi.org/10.1016/j.jallcom.2017.12.091
0925-8388/© 2017 Elsevier B.V. All rights reserved.

conductive CNFs can not only buffer the volume expansion in the charge/discharge processes, but also improve the electrical conductivity, which combines the their advantages together and leads to enhanced electrochemical performance [15–17].

Great efforts have been devoted to developing a various of nanostructured TMOs/CNFs composites with the assistance of electrospinning technology. For instance, Huang et al. [18] developed a MnO/CNFs composite by electrospinning of Mn_3O_4 nanoparticles into CNFs with subsequent H_2 reduction. The MnO/CNFs delivered a reversible capacity of about 750 mA h g^{-1} after 200 cycles at a current density of 200 mA g^{-1}. Kim et al. [19] electrospun cobalt salt into CNFs and obtained Co_3O_4/PCNF with subsequent two-step thermal treatment. The Co_3O_4/PCNF exhibited an excellent capacity of 952 mA h g^{-1} after 100 cycles at 100 mA g^{-1}. Kang et al. [7] dispersed hollow Fe_2O_3 spheres on amorphous carbon matrix to produce Fe_2O_3-C composite nanofibers via electrospinning and achieved a remarkable 812 mA h g^{-1} after 300 cycles at 1000 mA g^{-1}. Due to low cost, abundant resources, considerable theoretical capacity (978 mA h g^{-1}) [20], as well as versatile properties [21–23], ZnO has attracted much attention and been electrospun into CNFs to fabricate ZnO/CNFs and mixed TMOs/CNFs [24–29]. In the TMOs/CNFs composites, CNFs can accommodate the volume change of TMOs and provide conductive channels for electron transport along the longitudinal direction, resulting in good electrochemical performance. Nevertheless, the electron-transporting property and interactions between the nanofibers are not satisfied. Therefore, enhancing the interconnection between the CNFs is supposed to further improve the capacity and stability of TMOs/CNFs-based anode for LIBs applications.

Herein, we demonstrate a novel and facile strategy to prepare 3D interconnected ZnO/carbon nanofibers films as enhanced free-standing anode for lithium-ion batteries (LIBs). ZnO/CNFs composite is synthesized via one-step electrospinning of polyacrylonitrile and zinc acetate dehydrate. Petroleum asphalt (PA) is chosen as a carbon processor and intercalated into the ZnO/CNFs interspaces by solvent impregnation. Through subsequent two-step thermal treatments, PA-carbon layer is generated as interconnection and binder between the nanofibers, as well as covering layer for the ZnO nanocrystals. The addition amount of PA is also optimized. Owing to the novel 3D conductive network and reinforced nanostructure, the prepared ZnO/CNFs-PA films are evaluated as enhanced free-standing anode material with promoted electrochemical lithium-storage performance. The prepared ZnO/CNFs-PA films deliver high reversible capacity, good cycling stability and excellent rate performance.

2. Experimental

2.1. Synthesis of ZnO/CNFs-PA films

All reagents used were of analytical grade and used without any purification. In a typical synthesis procedure, 2.0 g polyacrylonitrile (PAN) and 2.0 g zinc acetate dehydrate [$Zn(CH_3COO)_2{\cdot}2H_2O$] were dissolved in 20 mL *N,N*-Dimethylformamide (DMF) and stirred for 12 h to make a homogeneous viscous gray dispersion for the electrospinning. The mixture was transferred into a plastic injector and electrospun on a spinning machine at a voltage of 22 kV. The propelling rate of injector was set as 20 μmL s^{-1}. The distance between the collecting cylinder (rotary speed 400 r min^{-1}) and the spinning needle was 15 cm to collect a flexible as-spun ZnO/CNFs precursor film. Petroleum asphalt (PA) was dispersed in toluene to form a 10 wt% solution. The obtained ZnO/CNFs precursor was impregnated in the PA solution for 6 h at room temperature. The whole vessel was moved into an oven and dried under 100 °C for removing the toluene solvent to obtain ZnO/CNFs-PA precursor. The prepared ZnO/CNFs-PA precursor was then pre-oxidized and stabilized at 240 °C in open air for 2 h to obtain ZnO/CNFs-PA pre-oxidized. Subsequently, the temperature was raised to 600 °C under a heating rate of 3 °C min^{-1} in nitrogen atmosphere and maintained for another 2 h to achieve the designed ZnO/CNFs-PA composite. To investigate the influence of PA addition amount, ZnO/CNFs-PA-0.4, ZnO/CNFs-PA-0.6, ZnO/CNFs-PA-1.0, ZnO/CNFs-PA-1.3 and ZnO/CNFs-PA-3.0 films were prepared by adjusting the PA amount to 0.4 g, 0.6 g, 1.3 g and 3.0 g, respectively. As a control, ZnO/CNFs was prepared with the same procedure without the addition of PA. Pure CNFs was also prepared by directly pre-oxidation and carbonization of the as-spun nanofibers derived from PAN.

2.2. Characterization

Fourier transform infrared (FT-IR) spectra were measured with a Nicolet Nexus FTIR spectrometer using the KBr pellet technique (Thermo Nicolet Nexus 670, USA). The crystal structure of the samples was characterized with X-ray diffraction (XRD) (X'Pert PRO MPD, Holland) using Cu Kα radiation (k = 1.518 Å) in angle of 2 theta from 10° to 78°. Scanning electron microscopic (SEM) images were recorded using a Hitachi S-4800 instrument. Thermal gravimetric analysis (TGA) was conducted in air at a heating rate of 5 °C min^{-1} (STA 409 PC Luxx, Germany). Element analysis was carried out with Element Vario EL III (Elementar Analysensysteme GmbH, Germany) analyzer.

2.3. Electrochemical measurements

The as-prepared ZnO/CNFs-PA films were directly used as free-standing working anode for LIBs. The electrochemical performance of the ZnO/CNFs-PA films were examined using CR2032 coin type cells vs. Li with 1 M $LiPF_6$ in ethylene carbonate/dimethyl carbonate (1:1 by volume) and Celgard 2300 membrane as the separator. The discharge and charge processes of the cells were tested using a Land CT2001A battery test system over a voltage range of 0.01–3.00 V *vs.* Li/Li^+. The cyclic voltammetry (CV) test was conducted on a CHI760E electrochemical workstation in the range of 0.01–3.00 V at a scan rate of 0.1 mV s^{-1}. Electrochemical impedance spectroscopy (EIS) tests were also performed on a CHI760E electrochemistry workstation in the frequency range of 100 KHz to 10 MHz with AC voltage amplitude 10 mV.

3. Results and discussion

The ZnO/CNFs-PA composites are synthesized by a feasible method as illustrated in Scheme 1 below. Polyacrylonitrile (PAN) and zinc acetate dehydrate [$Zn(OAc)_2{\cdot}2H_2O$] are chosen as raw material for electrospinning. Zinc salt doped CNFs precursor (ZnO/CNFs precursor) is firstly synthesized through one-step electrospinning of PAN and $Zn(OAc)_2{\cdot}2H_2O$, employing DMF as the solvent. Then the low-cost and viscous petroleum asphalt (PA) is intercalated into the CNFs interspaces and wrapped around the nanofiber surface for its high viscidity. The prepared ZnO/CNFs-PA precursor is then pre-oxidized and stabilized at 240 °C in open air. In this stage, PA is gradually softened and melted under such high temperature. The light components are volatilized, and the heavy components tend to be partially oxidized and polycondensed, forming a PA-carbon skeleton between and around the nanofibers. Then under a heating rate of 3 °C min^{-1} in nitrogen atmosphere, the temperature is raised to 600 °C to calcinate the sample. The PAN nanofiber precursor is carbonized, with ZnO

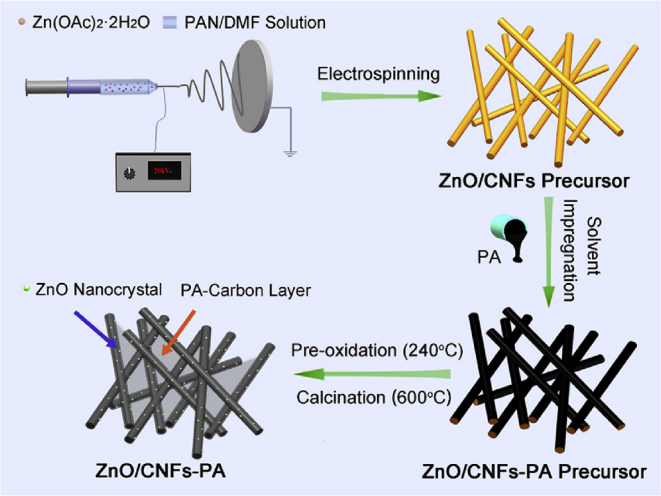

Scheme 1. Illustration for the synthesis of ZnO/CNFs-PA composites.

nanocrystals simultaneously synthesized and located on CNFs surface. In this procedure, the partially oxidized PA-carbon layer is further deoxidized, polycondensed and carbonized, generating a carbon layer between and around the CNFs. Thus free-standing ZnO/CNFs-PA films are obtained, which can be directly utilized as efficient anode materials for LIBs.

Fig. 1 shows the Fourier transform infrared (FT-IR) spectra of the ZnO/CNFs precursor, ZnO/CNFs-PA pre-oxidized and ZnO/CNFs-PA. ZnO/CNFs precursor is composed of PAN and $Zn(OAc)_2$. The doublet at 2925 and 2854 cm^{-1} and the peak at 1450 cm^{-1} correspond to stretching and bending vibrations of C-H, respectively. Characteristic stretching vibrations of C≡N can be observed at 2240 cm^{-1}. The strong peak at 1585 cm^{-1} and weak peak at 1735 cm^{-1} are associated with the carboxylate radical (O=C-O$^-$) groups in $Zn(OAc)_2$. After pre-oxidization treatment, the C≡N peak decreases, whereas new peaks at 1707 cm^{-1} corresponding to C=N and 810 cm^{-1} for aromatic heterocyclic ring (C=C-H) absorption appear, revealing the formation of aromatic structures and cyclization reactions in the per-oxidation stage. Compared with that of ZnO/CNFs-PA pre-oxidized, FTIR spectrum of ZnO/CNFs-PA reveals disappearance of the C-H, C≡N, O=C-O$^-$ adsorptions. In the meanwhile, the appearance of the in-plane vibrations of sp^2-hybridized C=C peak at 1560 cm^{-1} and C-C peak at 1235 cm^{-1} implies removal of the functional groups and successful carbonization. The broad peak at around 1130 cm^{-1} is ascribed to the C-N absorbance, suggesting nitrogen doping of ZnO/CNFs-PA derived from PAN and PA.

X-ray diffraction (XRD) was employed to determine the crystalline structure and chemical components of the composites. For comparison, Fig. 2a shows the XRD patterns of pure CNFs, ZnO/CNFs and ZnO/CNFs-PA. In the spectrum of pure CNFs, a broad diffraction peak assigned to characteristic (002) and (001) reflections of graphite can be seen at 24° and 44°, suggesting the existence of large amount of amorphous carbon [30]. As to ZnO/CNFs, besides the (002) reflection of carbon at 24°, characteristic peaks at 31.8°, 34.4°,36.3°, 47.5°, 56.6°, 62.9° and 68.0° are indexed to the (100), (002), (101), (102), (110), (103) and (112) crystal planes of the hexagonal ZnO crystalline structure. This result is in consistent with the standard ZnO card (JCPDS 36-1451) [31], revealing the formation of ZnO nanocrystals. When PA is intercalated, the pattern of ZnO/CNFs-PA shows no much difference with that of ZnO/CNFs. According to the Debye–Scherrer equation, the mean ZnO nanocrystals sizes of ZnO/CNFs and ZnO/CNFs-PA are calculated to be 15 nm and 17 nm, respectively. Therefore, ZnO nanocrystals with average dimeter less than 20 nm are synthesized in ZnO/CNFs-PA composite, and intercalation of PA will not influence the nanostructure of ZnO nanocrystals.

To further investigate the nanostructure and microtopography of ZnO/CNFs-PA samples, especially the influence of PA addition amount, scanning electron microscope (SEM) tests were further conducted. Fig. 3 shows SEM images of ZnO/CNFs, ZnO/CNFs-PA-0.4, ZnO/CNFs-PA-1.0 and ZnO/CNFs-PA-3.0. The ZnO/CNFs image shows nanofibers of uniform diameters around 150 nm, with ZnO nanocrystals (about 10–30 nm) homogenously depositing on the surface. The ZnO nanocrystals size is in good agreement with the above XRD result. When PA (mass ratio of 0.4) is added, the ZnO/CNFs-PA-0.4 exhibits smooth nanofibers partially interconnected by a PA-carbon layer. Probably due to partial PA agglomeration in the calcination process, some carbon nanoparticles with irregular shape and size can also be observed on the nanofiber surface. Whereas ZnO cannot be observed, suggesting that the nanocrystals are covered by the introducing PA-carbon layer. Fig. 3c shows the nanofibers of ZnO/CNFs-PA-1.0 are sufficiently interconnected with each other by the PA-carbon layer,

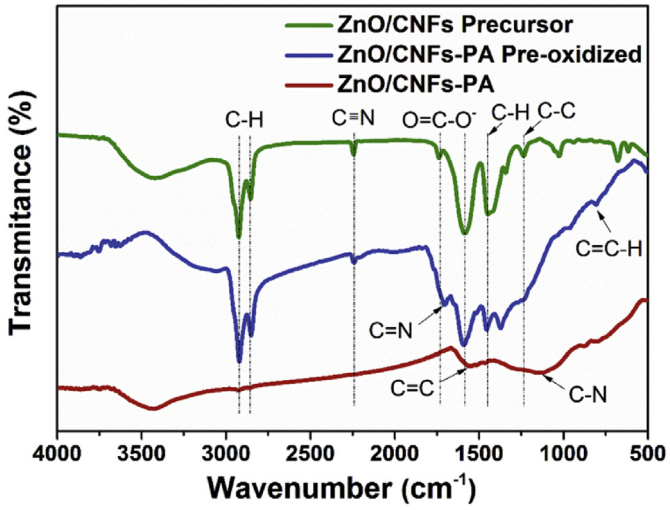

Fig. 1. FT-IR spectra of ZnO/CNFs precursor, ZnO/CNFs-PA pre-oxidized and ZnO/CNFs-PA.

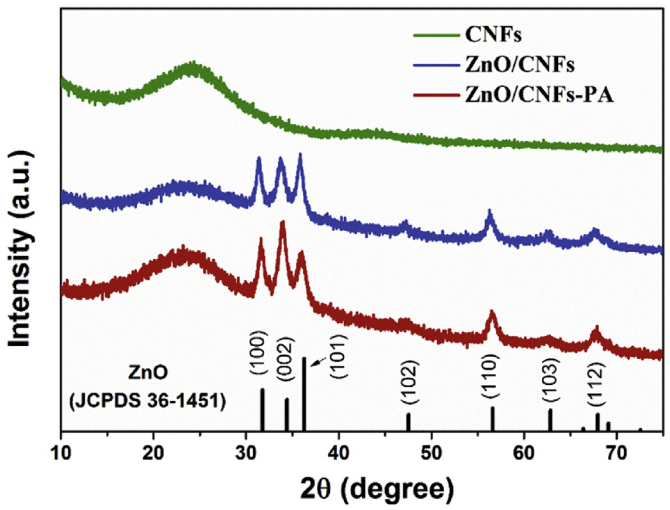

Fig. 2. XRD patterns of pure CNFs, ZnO/CNFs and ZnO/CNFs-PA.

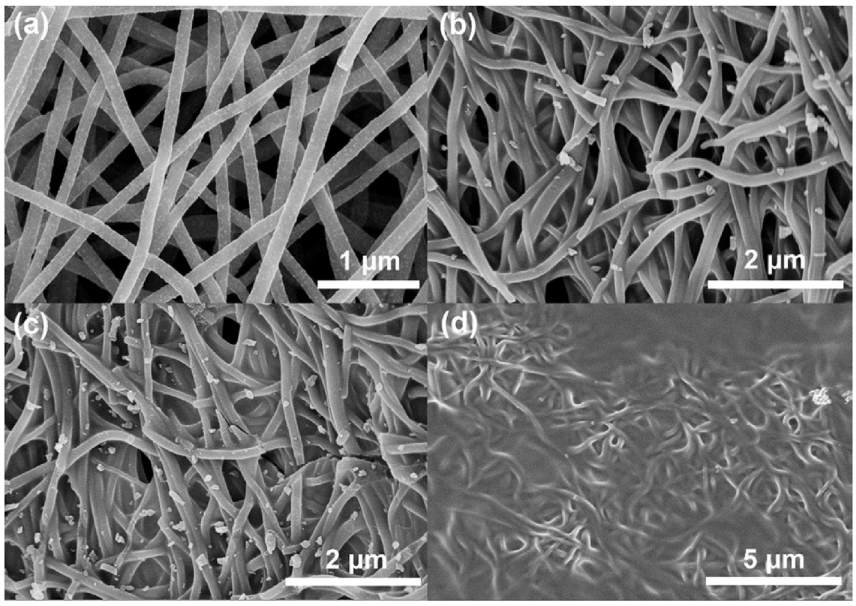

Fig. 3. SEM images of (a) ZnO/CNFs, (b) ZnO/CNFs-PA-0.4, (c) ZnO/CNFs-PA-1.0 and (d) ZnO/CNFs-PA-3.0.

constructing a 3D conductive network between the nanofibers. Meanwhile, some carbon nanoparticles with diameters around 150 nm are homogeneously distributed on the ZnO/CNFs-PA surface, which can also provide efficient lithium storage sites when used as LIBs anode. However, when the mass ratio of PA is raised to 3.0, the nanofibers are completely covered by excess PA without any pores (as shown in Fig. 3d), which will hinder the diffusion of the electrolyte and lithium ions, leading to inferior electrochemical activity. Comparison of the above results reveals that the PA addition amount is an essential factor to affect the microtopography of ZnO/CNFs-PA. Among them, ZnO/CNFs-PA-1.0 displays the optimal proportion and microstructure.

Since ZnO/CNFs-PA-1.0 shows the best nanostructure, thermal gravimetric analysis (TGA) was conducted in air at a heating rate of 5 °C min^{-1} to determine the ZnO content (Fig. 4). The sample starts to lose weight along with temperature rising. The weight loss before 200 °C should be ascribed to water gasification. The main weight loss occurs between 400 °C and 500 °C, arising from the carbon pyrolysis. After heating to 600 °C, the ZnO/CNFs-PA-1.0 is completely converted to ZnO. Accordingly, the mass percentages of ZnO is calculated to be 34.1 wt%. The composition of ZnO/CNFs-PA-1.0 is also detected by element analysis. The weight ratios of H, C, N and ZnO in ZnO/CNFs-PA-1.0 by element analysis are evaluated to be 1.8, 52.5, 10.5 and 35.2 wt %, respectively, which is in good agreement with the TGA result.

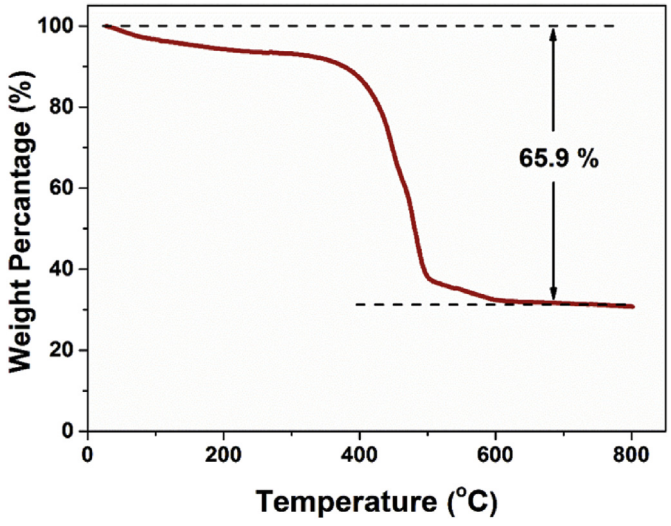

Fig. 4. TGA curve of ZnO/CNFs-PA-1.0 sample.

The characterization results reveal the successful intercalation of PA into ZnO/CNFs to fabricate 3D interconnected nanofiber composites. The obtained ZnO/CNFs-PA composites are free-standing films and can be directly utilized as anode for LIBs without any binder or current collector. Coin cells were made to evaluate the electrochemical properties of the samples. To uncover the charge/discharge mechanism, cyclic voltammetry (CV) test of ZnO/CNFs-PA-1.0 was firstly performed in 0.01–3.0 V voltage range at a 0.1 mV s^{-1} scan rate (Fig. 5a). ZnO/CNFs-PA-1.0 shows a peak at 1.4 V and vanishes in the following cycles, corresponding to irreversible lithium insertion into ZnO in the initial cycle [32]. The strong broad cathodic peaks between 0.3 V and 0.8 V reveal the reducing of ZnO to Zn and Li_2O, the alloying reaction between Zn and Li^+ to form Li_xZn, as well as the formation of solid electrolyte interface (SEI) layer [33–35]. Insertion of lithium into amorphous carbon can also be observed from the reduction peak at around 0.01 V [32]. In the anodic cycle, weak peaks at 0.3 V, 0.5 V and 0.7 V can be carefully discerned which are attributed to a multistep dealloying of Li_xZn alloy [33]. Another broad peak located at about 1.3 V corresponds to the redox reaction between Zn and Li_2O to form ZnO. In the following cycles, the CV curves coincide with each other, indicating the good reversibility in the charge/discharge cycles. Fig. 5b shows the galvanostatic charge/discharge curve of ZnO/CNFs-PA-1.0 at a current density of 200 mA g^{-1} between 0.01 and 3.0 V (*vs.* Li^+/Li). The initial discharge and charge capacities are 1664 and 801 mA h g^{-1}, respectively, with a relatively low Coulombic efficiency of 48.1%. As discussed above, the low Coulombic efficiency should mainly be caused by the irreversible lithium insertion into ZnO and formation of SEI layer on the surface of the nanofibers, which is common for most anode materials, especially nanostructured ones [36–39]. As with the CV result, a gradually

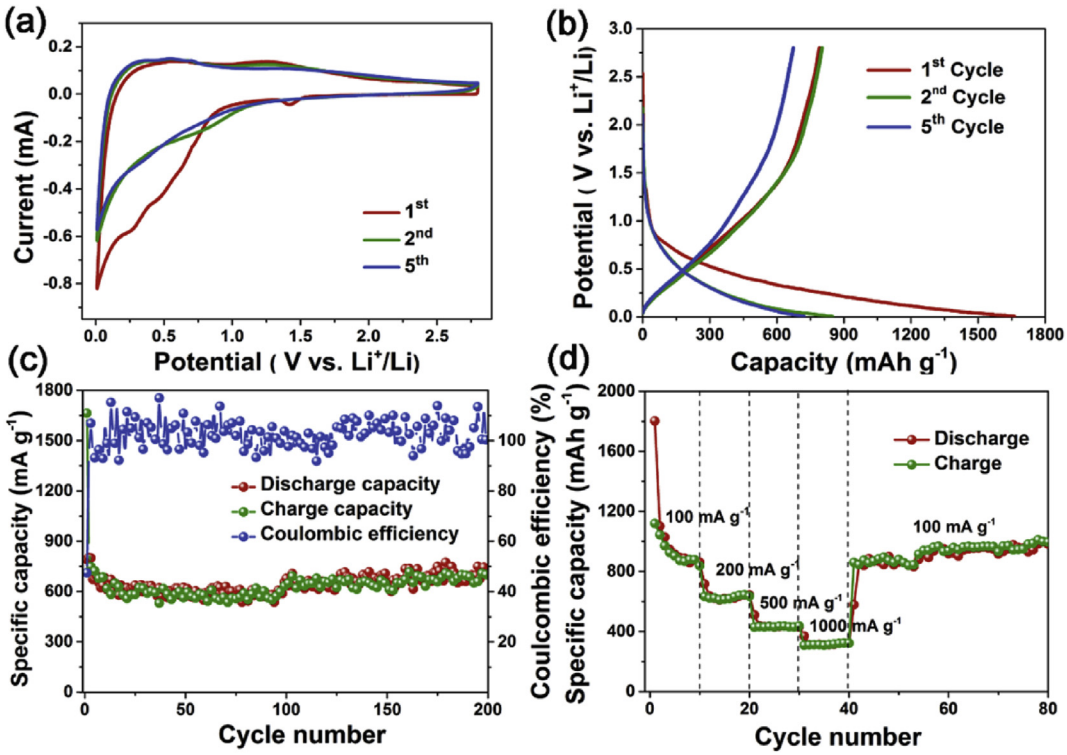

Fig. 5. (a) CV curve of ZnO/CNFs-PA-1.0. (b) Galvanostatic charge/discharge voltage profiles and (c) cyclic performance of ZnO/CNFs-PA-1.0 at a current density of 200 mA g^{-1}. (d) Rate performance of ZnO/CNFs-PA-1.0 and subsequent cyclic tests at a current density of 100 mA g^{-1}.

decrease discharge voltage plateaus below 0.8 V can be observed during the first discharge process. In the 5th cycle, the discharge and charge capacities are 722 and 676 mA h g^{-1}, respectively, delivering an increased Coulombic efficiency of 94%. Then cyclic performance test of ZnO/CNFs-PA-1.0 was conducted at a current density of 200 mA g^{-1}. As shown in Fig. 5c, the ZnO/CNFs-PA-1.0 sample shows a large capacity fading in the first ten cycles due to the formation of SEI film [40]. In the subsequent cycles, the electrode exhibits comparatively good stability, and the Columbic efficiencies are around 100%. After 200 cycles, ZnO/CNFs-PA-1.0 delivers a discharge and charge capacities are 702 mA h g^{-1} and 700 mA h g^{-1}, with nearly 100% Columbic efficiency.

Moreover, ZnO/CNFs-PA-1.0 also exhibits excellent rate performance, as shown in Fig. 5d. The electrode delivers a high specific capacity of 860 mA h g^{-1} at a current density of 100 mA g^{-1}. As the current densities are changed to 200, 500 and 1000 mA g^{-1}, the ZnO/CNFs-PA-1.0 shows high reversible capacities of 643, 431, and 323 mA h g^{-1}, respectively. Notably, when the current density is adjusted back to 100 mA g^{-1}, the electrode displays a specific capacity of 861 mA h g^{-1}, which is in full accord with the initial cycle. Then the capacity gradually goes up to an outstanding reversible capacity of 995 mA h g^{-1} with another 40 cycles, which is even higher than the theoretical value of ZnO anode. This remarkable capacity rise should be attributed to the release of additional Li^+ ions with increasing number of cycles and "pseudo-capacitance" behavior [41].

In order to investigate influence of the intercalated PA on the electrochemical performance, long-term cyclic performance tests of ZnO/CNFs-PA films with different PA addition amount were conducted (Fig. 6a). For comparison, long-term cyclic performance of ZnO/CNFs was also evaluated. ZnO/CNFs shows an initial discharge capacity of 1188 mA h g^{-1} and large attenuation in the first several cycles. With increasing cycles, the capacities are relatively stable. ZnO/CNFs achieves a reversible capacity of

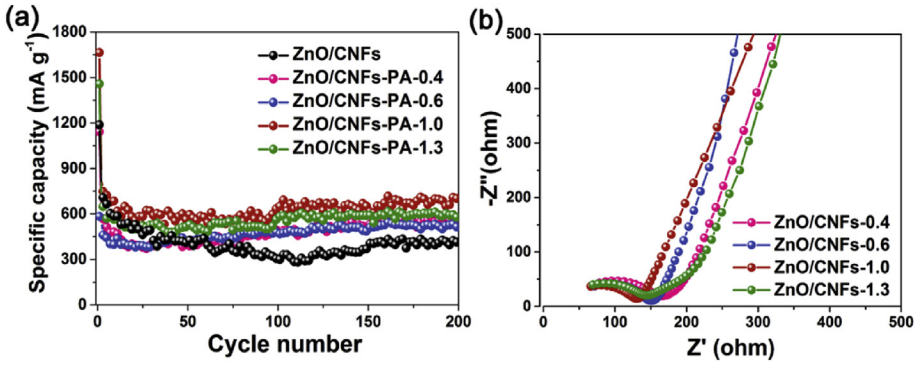

Fig. 6. (a) Long-term cyclic performance tests of ZnO/CNFs and ZnO/CNFs-PA samples. (b) Nyquist plots of ZnO/CNFs-PA samples.

403 mA h g^{-1} after 200 cycles. In comparison, the ZnO/CNFs-PA electrodes show much more stable cycling performance and higher capacities. After 200 cycles, the ZnO/CNFs-PA-0.4, ZnO/CNFs-PA-0.6, ZnO/CNFs-PA-1.0 and ZnO/CNFs-PA-1.3 samples deliver reversible capacities of 520, 552, 702 and 600 mA h g^{-1}, respectively. The superior stability and capacity should be ascribed to the formation of the 3D conductive network by the PA-carbon layer. Such structure can accommodate the volume expansion of ZnO, provide promoted electrical conductivity, and reinforce the electrode during long-term cycling processes [42–44]. Besides, with the increasing of PA addition amount, the capacity falls after increases first. This result suggests that appropriate PA would enhance the connections between the nanofibers. Nevertheless, excessive PA will block the interspace pores and results in overlarge electrolyte and Li^+ ions transfer resistance. To verify this speculation, electrochemical impedance spectroscopy (EIS) measurements of the ZnO/CNFs-PA films were carried out. A semicircle in high to middle frequency region and a straight line in low frequency region can be seen from the Nyquist plots of the ZnO/CNFs-PA samples in Fig. 6b. The diameter of the semicircle indicates the Li^+ migration resistance through the SEI film (Rs) and the charge-transfer resistance (Rc). The sloping straight line to the real impedance axis in the low frequency region, which represents Li^+ ions diffusion in the bulk of the electrode. The semicircle at high frequency can be assigned to the charge-transfer resistance (Rc) and the SEI film resistance (Rs) [34,45]. The sloping straight line to the real impedance axis in the low frequency region, which represents Li^+ ions diffusion in the bulk of the electrode. As can be seen, the Rc and Rs resistances of the samples follows the order of ZnO/CNFs-PA-0.4 > ZnO/CNFs-PA-0.6 > ZnO/CNFs-PA-1.3 > ZnO/CNFs-PA-1.0. This result is completely consistent with our inference associating with their different electrochemical performance. Among them, ZnO/CNFs-PA-1.0 stands out and displays the optimal PA additional proportion. However, as expected, the inclined line at low frequency of ZnO/CNFs-PA-1.0 shows a smaller slope compared with ZnO/CNFs-PA-0.4 and ZnO/CNFs-PA-0.6, suggesting that the intercalation of PA will slightly hinder the lithium diffusion process within the electrodes.

The above results indicate the ZnO/CNFs-PA-1.0 possesses enhanced conductivity and reinforced nanostructure, leading to the improvement of electrochemical performance. By intercalating of PA into electrospun ZnO/CNFs, the nanofibers and PA-carbon layer fabricate a 3D conductive network. Such unique nanostructure creates shorter diffusion paths for Li^+ ions in the electrolyte, provides high-speed road for charge transfer and reinforces the electrode material. Moreover, the *in-situ* formed ZnO nanocrystals are covered by the PA-carbon layer, which can effectively accommodate the volume expansion of ZnO during the cycling process. Therefore, the conductive and viscous PA serves as potential interconnection for electrospun ZnO/CNFs to achieve enhanced self-standing LIBs electrode materials with promoted reversible capacity and excellent cyclability.

4. Conclusions

In summary, we successfully developed a novel strategy to construct ZnO/CNFs-PA films as enhanced free-standing anode for LIBs. Through solvent impregnation and subsequent two-step thermal treatments, appropriate amount of petroleum asphalt is intercalated into ZnO/CNFs to generate a conductive PA-carbon film between nanofibers, as well as covering layer of the ZnO nanocrystals. Benefiting from the special 3D conductive network structure, which can effectively accommodate the volume expansion of ZnO, facilitate charge transfer and reinforce the electrode, the ZnO/CNFs-PA-1.0 composite delivers promoted reversible capacity of 702 mA h g^{-1} at 200 mA g^{-1} after 200 cycles, associating with excellent rate capability and cyclic stability. This work may open up a feasible and cost-effective avenue to produce transition metal oxide/carbon nanofibers electrodes with superior electrochemical performance and industrial potential for LIBs.

Acknowledgements

This work was supported by the National Natural Science Foundation of China (Nos. 51372277, 51572296, U1662113); the Shandong Provincial Natural Science Foundation (ZR2016BB18); the Fundamental Research Fund for the Central Universities (No. 18CX02015A, 15CX08005A, 14CX02127A); the China Postdoctoral Science Foundation (2016M592268).

References

[1] M.R. Palacin, Recent advances in rechargeable battery materials: a chemist's perspective, Chem. Soc. Rev. 38 (2009) 2565–2575.
[2] J. Cabana, L. Monconduit, D. Larcher, M.R. Palacin, Beyond intercalation-based Li-Ion batteries: the state of the art and challenges of electrode materials reacting through conversion reactions, Adv. Mater. 22 (2010) E170–E192.
[3] Q. Wei, F. Xiong, S. Tan, L. Huang, E.H. Lan, B. Dunn, L. Mai, Porous one-dimensional nanomaterials: design, fabrication and applications in electrochemical energy storage, Adv. Mater. 29 (2017), 1602300.
[4] Y.M. Chen, X.Y. Yu, Z. Li, U. Paik, D. Lou, Hierarchical MoS_2 tubular structures internally wired by carbon nanotubes as a highly stable anode material for lithium-ion batteries, Adv.Sci. 2 (2016), e1600021.
[5] Y. Liu, D. Guan, G. Gao, X. Liang, W. Sun, K. Zhang, W. Bi, G. Wu, Enhanced electrochemical performance of electrospun V_2O_5 nanotubes as cathodes for lithium ion batteries, J. Alloys Compd. (2017), https://doi.org/10.1016/j.jallcom.2017.07.214.
[6] J. Jin, Z. Shi, C. Wang, Electrochemical performance of electrospun carbon nanofibers as free-standing and binder-free anodes for sodium-ion and lithium-ion batteries, Electrochim. Acta 141 (2014) 302–310.
[7] J.S. Cho, Y.J. Hong, Y.C. Kang, Design and synthesis of bubble-nanorod-structured Fe_2O_3–Carbon nanofibers as advanced anode material for Li-Ion batteries, ACS Nano 9 (2015) 4026–4035.
[8] L. Zhang, A. Aboagye, A. Kelkar, C. Lai, H. Fong, A review: carbon nanofibers from electrospun polyacrylonitrile and their applications, J. Mater. Sci. 49 (2014) 463–480.
[9] V. Aravindan, J. Sundaramurthy, P.S. Kumar, Y. Lee, S. Ramakrishna, S. Madhavi, Electrospun nanofibers: a prospective electro-active material for constructing high performance Li-Ion batteries, Chem. Commun. 51 (2015) 2225–2234.
[10] S. Cavaliere, S. Subianto, I. Savych, D.J. Jones, J. Roziere, Electrospinning: designed architectures for energy conversion and storage devices, Energ. Environ. Sci. 4 (2011) 4761–4785.
[11] Z. Li, J. Zhang, L. Yu, J. Zhang, Electrospun porous nanofibers for electrochemical energy storage, J. Mater. Sci. 52 (2017) 6173–6195.
[12] S. Peng, L. Li, Y. Hu, M. Srinivasan, F. Cheng, J. Chen, S. Ramakrishna, Fabrication of spinel one-dimensional architectures by single-spinneret electrospinning for energy storage applications, ACS Nano 9 (2015) 1945–1954.
[13] C. Liang, M. Gao, H. Pan, Y. Liu, M. Yan, Lithium alloys and metal oxides as high-capacity anode materials for lithium-ion batteries, J. Alloys Compd. 575 (2013) 246–256.
[14] C. Zhang, S. Yu, Nanoparticles meet electrospinning: recent advances and future prospects, Chem. Soc. Rev. 43 (2014) 4423–4448.
[15] S. Ding, J.S. Chen, One-dimensional hierarchical structures composed of novel metal oxide nanosheets on a carbon nanotube backbone and their lithium-storage properties, Adv. Funct. Mater. 21 (2011) 4120–4125.
[16] M. Reddy, G. Subba Rao, B. Chowdari, Metal oxides and oxysalts as anode materials for Li ion batteries, Chem. Rev. 113 (2013) 5364–5457.
[17] H.B. Wu, G. Zhang, L. Yu, X.W.D. Lou, One-dimensional metal oxide–carbon hybrid nanostructures for electrochemical energy storage, Nanoscale Horiz. 1 (2016) 27–40.
[18] B. Liu, X. Hu, H. Xu, W. Luo, Y. Sun, Y. Huang, Encapsulation of MnO nanocrystals in electrospun carbon nanofibers as high-performance anode materials for lithium-ion batteries, Sci. Rep. 4 (2014) 4229.
[19] S. Abouali, M.A. Garakani, B. Zhang, H. Luo, Z. Xu, J. Huang, J. Huang, J. Kim, Co_3O_4/Porous electrospun carbon nanofibers as anodes for high performance Li-Ion batteries, J. Mater. Chem. A 2 (2014) 16939–16944.
[20] M. Laurenti, N. Garino, S. Porro, M. Fontana, C. Gerbaldi, Zinc oxide nanostructures by chemical vapour deposition as anodes for Li-Ion batteries, J. Alloys Compd. 640 (2015) 321–326.
[21] C. Li, Z. Zang, C. Han, Z. Hu, X. Tang, J. Du, Y. Leng, K. Sun, Highly compact $CsPbBr_3$ perovskite thin films decorated by ZnO nanoparticles for enhanced random lasing, Nanomater. Energy 40 (2017) 195–202.

[22] C. Li, C. Han, Y. Zhang, Z. Zang, M. Wang, X. Tang, J. Du, Enhanced photoresponse of self-powered perovskite photodetector based on ZnO nanoparticles decorated $CsPbBr_3$ films, Sol. Energy Mater. Sol. Cell. 172 (2017) 341–346.
[23] W. Hu, H. Wei, Y. She, X. Tang, M. Zhou, Z. Zang, J. Du, C. Gao, Y. Guo, D. Bao, Flower-like nickel-zinc-cobalt mixed metal oxide nanowire arrays for electrochemical capacitor applications, J. Alloys Compd. 708 (2017).
[24] P. Li, Y. Liu, J. Liu, Z. Li, G. Wu, M. Wu, Facile synthesis of ZnO/mesoporous carbon nanocomposites as high-performance anode for lithium-ion battery, Chem. Eng. J. 271 (2015) 173–179.
[25] S.Y. Kim, B.-H. Kim, Electrochemical performance of activated carbon nanofiber with ZnO nanoparticles for Li-Ion battery, Synth. Met. 210 (2015) 386–391.
[26] Y. Zhao, X. Li, L. Dong, B. Yan, H. Shan, D. Li, X. Sun, Electrospun SnO_2–ZnO nanofibers with improved electrochemical performance as anode materials for lithium-ion batteries, Int. J. Hydrogen Energy 40 (2015) 14338–14344.
[27] B.N. Joshi, S. An, H.S. Jo, K.Y. Song, H.G. Park, S. Hwang, S.S. Al-Deyab, W.Y. Yoon, S.S. Yoon, Flexible, freestanding, and binder-free SnO_x–ZnO/carbon nanofiber composites for lithium ion battery anodes, ACS Appl. Mater. Interfaces 8 (2016) 9446–9453.
[28] H. Ning, H. Xie, Q. Zhao, J. Liu, W. Tian, Y. Wang, M. Wu, Electrospinning ZnO/carbon nanofiber as binder-free and self-supported anode for Li-Ion batteries, J. Alloys Compd. 722 (2017) 716–720.
[29] B.M. Basavaraja, S.B. Majumder, A. Sharma, Electrospun hollow glassy carbon–reduced graphene oxide nanofibers with encapsulated ZnO nanoparticles: a free standing anode for Li-Ion batteries, J. Mater. Chem. A 3 (2015) 5344–5351.
[30] Y. Wang, Y. Wang, J. Liu, L. Pan, W. Tian, M. Wu, J. Qiu, Preparation of carbon nanosheets from petroleum asphalt via recyclable molten-salt method for superior lithium and sodium storage, Carbon 122 (2017) 344–351.
[31] G. Zhang, S. Hou, H. Zhang, W. Zeng, F. Yan, C.C. Li, H. Duan, High-performance and ultra-stable lithium-ion batteries based on MOF-derived ZnO@ ZnO quantum Dots/C core–shell nanorod arrays on a carbon cloth anode, Adv. Mater. 27 (2015) 2400–2405.
[32] M. Yu, A. Wang, Y. Wang, C. Li, G. Shi, An alumina stabilized ZnO–graphene anode for lithium ion batteries via atomic layer deposition, Nanoscale 6 (2014) 11419–11424.
[33] Q. Xie, X. Zhang, X. Wu, H. Wu, X. Liu, G. Yue, Y. Yang, D. Peng, Yolk-shell ZnO-C microspheres with enhanced electrochemical performance as anode material for lithium ion batteries, Electrochim. Acta 125 (2014) 659–665.
[34] Z. Ren, Z. Wang, C. Chen, J. Wang, X. Fu, C. Fan, G. Qian, Preparation of carbon-encapsulated ZnO tetrahedron as an anode material for ultralong cycle life performance lithium-ion batteries, Electrochim. Acta 146 (2014) 52–59.
[35] F. Sun, J. Gao, H. Wu, X. Liu, L. Wang, X. Pi, Y. Lu, Confined growth of small ZnO nanoparticles in a nitrogen-rich carbon framework: advanced anodes for long-life Li-Ion batteries, Carbon 113 (2017) 46–54.
[36] Y. Han, P. Qi, S. Li, X. Feng, J. Zhou, H. Li, S. Su, X. Li, B. Wang, A novel anode material derived from organic-coated ZIF-8 nanocomposites with high performance in lithium ion batteries, Chem. Commun. 50 (2014) 8057–8060.
[37] H. Yue, Z. Shi, Q. Wang, Z. Cao, H. Dong, Y. Qiao, Y. Yin, S. Yang, MOF-derived cobalt-doped ZnO@ C composites as a high-performance anode material for lithium-ion batteries, ACS Appl. Mater. Interfaces 6 (2014) 17067–17074.
[38] R. Guo, W. Yue, Y. An, Y. Ren, X. Yan, Graphene-encapsulated porous carbon-ZnO composites as high-performance anode materials for Li-Ion batteries, Electrochim. Acta 135 (2014) 161–167.
[39] Y. Song, Y. Chen, J. Wu, Y. Fu, R. Zhou, S. Chen, L. Wang, Hollow metal organic frameworks-derived porous ZnO/C nanocages as anode materials for lithium-ion batteries, J. Alloys Compd. 694 (2017) 1246–1253.
[40] N. Garino, A. Lamberti, R. Gazia, A. Chiodoni, C. Gerbaldi, Cycling behaviour of sponge-like nanostructured ZnO as thin-film Li-Ion battery anodes, J. Alloys Compd. 615 (2014) S454–S458.
[41] Q. Li, H. Zhang, S. Lou, Y. Qu, P. Zuo, Y. Ma, X. Cheng, C. Du, Y. Gao, G. Yin, Pseudocapacitive Li^+ intercalation in ZnO/ZnO@C composites enables high-rate lithium-ion storage and stable cyclability, Ceram. Int. 43 (2017) 11998–12004.
[42] Z. Bai, Y. Zhang, N. Fan, C. Guo, B. Tang, One-step synthesis of ZnO@C nanospheres and their enhanced performance for lithium-ion batteries, Mater. Lett. 119 (2014) 16–19.
[43] S. Gao, R. Fan, B. Li, L. Qiang, Y. Yang, Porous carbon-coated ZnO nanoparticles derived from low carbon content formic acid-based Zn (II) metal-organic frameworks towards long cycle lithium-ion anode material, Electrochim. Acta 215 (2016) 171–178.
[44] C. Hsieh, C. Lin, Y. Chen, J. Lin, Synthesis of ZnO@ graphene composites as anode materials for lithium ion batteries, Electrochim. Acta 111 (2013) 359–365.
[45] X. Shen, D. Mu, S. Chen, B. Wu, F. Wu, Enhanced electrochemical performance of ZnO-loaded/porous carbon composite as anode materials for lithium ion batteries, ACS Appl. Mater. Interfaces 5 (2013) 3118–3125.